Molecular dynamics simulation study of nanoscale passive oxide growth on Ni-Al alloy surfaces at low temperatures

Subramanian K. R. S. Sankaranarayanan and Shriram Ramanathan*

Harvard School of Engineering and Applied Sciences, Harvard University, Cambridge, Massachusetts 02138, USA

(Received 10 March 2008; revised manuscript received 11 June 2008; published 15 August 2008)

Oxidation kinetics of Ni-Al (100) alloy surface is investigated at low temperatures (300–600 K) and at different gas pressures using molecular dynamics (MD) simulations with dynamic charge transfer between atoms. Monte Carlo simulations employing the bond order simulation model are used to generate the surface segregated minimum energy initial alloy configurations for use in the MD simulations. In the simulated temperature-pressure-composition regime for Ni-Al alloys, we find that the oxide growth curves follow a logarithmic law beyond an initial transient regime. The oxidation rates for Ni-Al alloys were found to decrease with increasing Ni composition. Structure and dynamical correlations in the metal/oxide/gas environments are used to gain insights into the evolution and morphology of the growing oxide film. Oxidation of Ni-Al alloys is characterized by the absence of Ni-O bond formation. Oxide films formed on the various simulated metal surfaces are amorphous in nature and have a limiting thickness ranging from ~1.7 nm for pure Al to 1.1 nm for 15% Ni-Al surfaces. Oxide scale analysis indicates significant charge transfer as well as variation in the morphology and structure of the oxide film formed on pure Al and 5% Ni-Al alloy. For oxide scales thicker than 1 nm, the oxide structure in case of pure Al exhibits a mixed tetrahedral (AlO_4 ~ 37%) and octahedral (AlO_6 ~ 19%) environment, whereas the oxide scale on Ni-Al alloy surface is almost entirely composed of tetrahedral environment (AlO_4 ~ 60%) with very little AlO_6 (<1%). The oxide growth kinetic curves are fitted to Arrhenius-type plots to get an estimate of the activation energy barriers for metal oxidation. The activation energy barrier for oxidation on pure Al was found to be 0.3 eV lower than that on 5% Ni-Al surface. Atomistic observations as well as calculated dynamical correlation functions indicate a layer by layer growth on pure Al, whereas a transition from an initial island growth mode (<75 ps) to a layer by layer mode (>100 ps) occurs in case of 5% Ni-Al alloy. The oxide growth on both pure Al and Ni-Al alloy surfaces occurs by inward anion and outward cation diffusions. The cation diffusion in both the cases is similar, whereas the anion diffusion in case of 5% Ni-Al is 25% lower than pure Al, thereby resulting in reduced self-limiting thickness of oxide scale on the alloy surface. The simulation findings agree well with previously reported experimental observations of oxidation on Ni-Al alloy surface.

DOI: 10.1103/PhysRevB.78.085420 PACS number(s): 81.65.Mq, 81.16.Pr, 82.20.Wt, 81.05.Bx

I. INTRODUCTION

Oxidation of metal and metal alloy surfaces are of considerable technological interest and are important for numerous applications ranging from heterogeneous catalysis and microelectronics to protection against wear and corrosion.[1–5] Passive oxide films formed on aluminum and aluminum alloys in air offer protection against further oxidation and corrosion.[6–8] This passivation effect has been responsible for their successful use as engineering materials.[9] In particular, oxide films formed from metal alloys such as Ni-Al are known to offer enhanced corrosion resistance as compared to those formed from their single metal constituents.[10] Although many experimental studies have characterized the formation mechanism and microstructure of these oxide films, very little is known about the oxidation growth kinetics as well as atomistic details of the composition, microstructure, and the limiting thickness of the oxide films at the nanoscale, especially for alloys.[11–17]

The oxidation mechanism, as well as the structure of the metal oxide formed, and its evolution during growth on the metal surface can be studied using several different approaches. Theoretical approaches based on *ab initio* and density-functional theories (DFTs) have been primarily employed to study the initial stages of O_2 reaction with metal surfaces, the dissociation processes involved in oxidation, and the stability of the various adsorption sites (top, bridge, and hollow sites on fcc or hcp lattice).[18–25] However, these approaches are confined to very small system sizes and do not include the effect of thermal vibrations. Hence the dynamics associated with the oxide growth on metal surfaces may not be adequately modeled by these approaches. One of the alternatives to density-functional approach is *ab initio* molecular dynamics (MD). However, although *ab initio* molecular dynamics simulations have existed for over a decade, they have been mainly used to predict the complex structures of the oxide film resulting from oxidation on metal surfaces.[25,26] The kinetics of oxidation on metal surfaces, which involves several thousands of atoms has not been studied using *ab initio* molecular dynamics owing to its computationally intensive nature.[27] Atomistic simulations such as classical MD have proven to be a complementary tool for investigating the atomistic details of the growth mechanism as well as the evolution of the morphology and structure of the oxides formed on metal surfaces.[28–32] Additionally, classical MD simulations with semiempirical potential models make it possible to simulate much larger systems containing several thousands or even millions of atoms.

Most of the previous theoretical studies utilizing classical MD simulations have focused on understanding the oxida-

 ©2008 The American Physical Society

tion processes of pure metals mainly aluminum.[28–33] Gutierrez and Johansson[34] have investigated the structural properties of amorphous Al_2O_3 utilizing fixed atomic charges. They found the coordination number of the elementary oxide unit that was formed, increased with the oxide density. Although the fixed charge potential model allows for easy implementation in efficient MD algorithms, it has several shortcomings.[35] The fixed charge model does not allow the introduction of multiple oxidation states. Aluminum however can form different oxide compounds such as Al_2O_3 and AlO_x, where the charge on the ions is a function of the oxygen/aluminum ratio.[31] During the oxidation of metals, significant positive charges are induced on the metal atoms and significant negative charges are induced on the oxygen atoms. Hence, the charges induced on these atoms are environment dependent. For instance, the charges on metal atoms change continuously from a zero value in a fully metallic region to their valency determined maximum value in the stoichiometric oxide. Additionally, the fixed charge models cannot be used to study the structure of the interface between a metal and its oxide. Hence, a potential model, which can switch between one dominated by ionic interactions in the oxide regions and metallic interactions in the metal region, is required.[35,36]

The charge-transfer ionic potential (CTIP) approach was proposed by Rappe and Goddard[37] and later by Streitz and Mintmire[38] to allow environment dependent charges on the atoms to be dynamically deduced. This was utilized by Campbell and co-workers[30,31] in their molecular dynamics simulations of 800 nm diameter aluminum nanoclusters where the thickness of the oxide formed was found to saturate at 3–4 nm thickness. Hasnaoui *et al.*[28] investigated the oxidation of low index aluminum surfaces at low temperatures. The growth kinetics was found to follow a direct logarithmic law and the oxide structure was found to exhibit a tetrahedral environment (AlO_4) in the oxide interior and mixed tetrahedral and octahedral (AlO_6) environment in the outer oxide regions for oxide thickness $\sim$2 nm. In another investigation by Hasnaoui *et al.*,[29] the growth kinetics was found to be independent of the crystallographic orientation.

Although there have been several theoretical studies on the oxidation kinetics based on pure metal surfaces such as Al,[28–30] Pt,[39,40] and Cu,[41,42] the oxidation kinetics on alloy surfaces have been much less explored. The complex nature of the interatomic interactions makes it difficult to simulate oxidation of metal alloys and metal-oxide heterophase interfaces. Additionally, complex phenomena such as surface segregation and micromixing are known to occur in alloy systems and can significantly influence the morphology and composition of the alloy metal surface. The oxidation mechanism as well as oxide growth on such surfaces is then expected to be very different from those on elemental metal surfaces. In this work, we utilize molecular simulations to obtain insights into the oxidation kinetics and growth of passive oxide films on one such alloy surface i.e., Ni-Al. Although there have been several experimental studies on the high temperature as well as low-temperature oxidation of Ni-Al surfaces, very little is known about the oxidation mechanism and initial stages of oxide growth on Ni-Al surfaces.[43,44] In particular, there still exist doubts over the possibility of Ni-O bond formation in oxides formed on Ni-Al alloy.[45–47] The presence of metallic Ni at the oxidized surface has not been ruled out in low-temperature oxidation, whereas Ni atoms are suggested to be expelled from the surface of the ordering oxide overlayers at high temperatures.[48]

This represents one of the first theoretical work, which focuses on the oxidation mechanism and nanoscale oxide growth kinetics on alloy metal surfaces. In particular, the atomistic mechanism associated with the nanoscale oxide growth on Ni-Al alloy surface is explored in detail. The oxidation kinetics on Ni-Al alloy metal surfaces is studied using MD simulations. The modified CTIP (Ref. 49) model coupled with embedded atom method (EAM) (Ref. 50) is used for modeling the metal/metal oxide systems. This potential model allows for variable and dynamic charge transfer between atoms and overcomes the limitations imposed by Streitz-Mintmire potential function and is suitable to study oxidation process on alloy systems involving thousands of atoms. Our simulation of Ni-Al surfaces indicates that the oxidation kinetics and oxide growth are strongly dependent on the composition of the alloy. The rate of oxide growth and the self-limiting thickness of the oxide film are found to decrease with increasing composition of Ni in the Ni-Al alloys. Furthermore, the effects of temperature and gas pressure on the oxidation kinetics are also discussed. The activation energy barriers for oxidation on the metal surfaces are derived from the simulated oxidation kinetic curves. The atomic trajectories generated using MD simulations are also used to identify the diffusion mechanisms associated with the oxide growth. Structure and dynamical correlations in the metal/oxide/gas environments are used to gain insights into the evolution and morphology of the growing oxide film. Comparison of the oxidation kinetics and oxide growth on Ni-Al alloy surfaces to that on pure Al and Ni is also carried out.

II. INITIAL CONFIGURATION SETUP

For the range of alloy compositions (0%, 5%, 10%, 15%, and 100% Ni) simulated, transition elements such as Al and Ni exhibit an fcc structure in the bulk alloy solid phase.[51,52] A slab of fcc was formed from a fcc unit cell by replicating it in *ABC* directions. The surfaces were generated by artificially increasing the x direction and introducing two vacuum slabs on each side of the metal substrate. This unit cell shown in Fig. 1 was repeated infinitely though three-dimensional (3D) space by applying periodic boundary conditions. This configuration allows for accurate computation of the Coulomb interaction by the Ewald summation technique.[53]

In order to identify the initial atomic positions of the constituent atoms for a given bimetallic alloy composition, these surface structures were subjected to a Metropolis Monte Carlo (MC) simulation employing a bond order simulation (BOS) model,[54,55] to generate the minimum free-energy initial configuration, which was subsequently used for studying the oxidation process. The system energy (ΔE) is given in terms of the site energies (ε) of the atoms, which is a function of their coordination numbers.

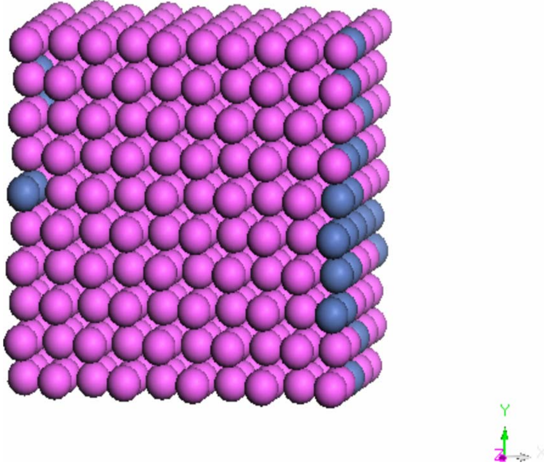

FIG. 1. (Color online) Sample initial alloy configuration (5% Ni-Al) generated by bond order simulation model.

$$\Delta E(\{A_i\}) = \sum_{i=1}^{N} \mathcal{E}_{Z_i}^{A_i,M_i \text{ of } B}, \tag{2.1}$$

where A_i is either A-type or B-type atom and ε is the site energy for an A-type atom surrounded by M of B type and total of Z neighbors. The site energies for the various different alloy systems including Al-Ni have been given by DePristo *et al.*[54–57] Thus, the state of the system is characterized by the energy of the system as given by Eq. (2.1). The system energy change was computed by swapping pairs of atoms of different types in the constructed fcc lattice and the standard Metropolis MC method was used to generate the minimum energy configuration at 300 K. Convergence was obtained when the minimum energy obtained during the simulation steps becomes constant ($\Delta E < 0.0001$) and the state of the system corresponding to that minimum energy was retained. Large number of simulations (99), with random initial configurations, each having (100 times the total number of atoms) steps were performed to ensure convergence. This was done to overcome any significant variations between different MC realizations and avoid any bias produced by a particular initial configuration.

The BOS mixing model developed by DePristo *et al.*[56] has been found to be very comprehensive in predicting the equilibrium structure of bimetallics. Developed from non-self-consistent electron-density-functional theory, the BOS model has been tested rigorously over a wide range of bimetallics.[54–57] Comparisons with experimental data reveal close agreements with the BOS model predicted microstructure.[54–56] This is the main motivation for using BOS in the present study to generate initial configurations. Qualitatively, similar segregation (as seen from the ratio of surface atoms to bulk for each metal) is predicted by the MC simulations using the EAM potential and the BOS model. However, based on previous investigations it was found that the equilibrium structure predicted by BOS-MC is slightly more stable than the one predicted by EAM-MC (energy comparisons).[58] Furthermore, the initial configuration generated by the BOS-MC model has been used previously in MD simulations employing EAM model to successfully predict the thermodynamic and mechanical properties of alloy systems. The details can be found in Refs. 58–63. Hence, the BOS model is consistent with the potential model used subsequently in the MD simulations. The BOS model was modified to have periodic boundary conditions along the y and z directions. The stable configurations generated in the above simulations consisted of surface segregated structures with Ni atoms segregating and preferentially locating themselves at the exposed faces (Fig. 1). The extent of segregation at any given temperature and alloy composition is dependent on the relative values of surface energies, mixing energy, and entropic factors. For increasing compositions of Ni, the surface composition of Ni atoms also showed an increase. A tendency for Ni-Al mixing at higher Ni compositions was also observed, which is consistent with the strong exothermic mixing in the alloys. These minimum energy configurations were utilized in the MD simulations to study the oxide growth kinetics.

III. COMPUTATIONAL DETAILS

The details of the potential function utilized in this work as well as the MD simulation details of the oxidation process are discussed in this section.

A. CTIP-EAM potential function

The MD simulation technique utilized in the present work is based on the modified charge-transfer potential model developed by Zhou and co-workers.[35,49] The interaction potential is divided into an electrostatic contribution (E_{es}) for ionic interactions and a nonelectrostatic energy (E_m) based on the alloy embedded atom method to model metal interactions.

$$E_t = E_{es} + E_m. \tag{3.1}$$

The modified charge-transfer potential model imposes charge bounds on the metal and gas atoms and prevents the atoms from exceeding their valence charges, thereby overcoming the limitations of the original Streitz-Mintmire potential.[38] The electrostatic energy used in the modified CTIP model is given below:[35]

$$E_{es} = E_0 + \sum_{i=1}^{N} q_i X_i + \frac{1}{2}\sum_{i=1}^{N}\sum_{j=1}^{N} q_i q_j V_{ij} + \sum_{i=1}^{N} \omega\left(1 - \frac{q_i - q_{\min,i}}{|q_i - q_{\min,i}|}\right) \times (q_i - q_{\min,i})^2 + \sum_{i=1}^{N} \omega\left(1 - \frac{q_{\max,i} - q_i}{|q_i - q_{\max,i}|}\right)(q_i - q_{\max,i})^2, \tag{3.2}$$

where $q_{\min,i}$ and $q_{\max,i}$ are the charge bounds of atom i, $q_{\min,i} < q_i < q_{\max,i}$. The coefficient ω corresponds to the energy penalty for the metal atoms to gain electrons or lose inner shell electrons or for the oxygen atoms to lose electrons or receive more than two electrons. X_i and V_{ij} are terms representing the self-energy and Coulomb interaction, respectively.[38] The charge parameters χ_i, J_i, ξ, and Z_i, as well as the charge bounds for the various elements, are listed in Table I.

TABLE I. CTIP parameters for the simulated elements (based on Zhou *et al.* Ref. 64).

Element	$q_{\min}$	$q_{\max}$	χ (eV)	J (eV)	ξ (Å^{-1})	Z (e)
O	−2	0	2.00000	14.99523	0.00000	02.144
Al	0	3	1.47914	9.07222	0.968	1.07514
Ni	0	2	−1.70804	9.10954	1.087	1.44450

The nonelectrostatic interactions, which occur between the metal atoms can be modeled using the EAM. The nonelectrostatic energy is expressed as:[50]

$$E_m = \frac{1}{2}\sum_{i=1}^{N}\sum_{j=i_1}^{i_N}\phi_{ij}(r_{ij}) + \sum_{i=1}^{N}F_i(\rho_i), \tag{3.3}$$

where $\varphi_{ij}(r_{ij})$ represents the pairwise interaction energy between atoms i and j separated by distance r_{ij}. The generalized elemental pair potentials for the alloy systems are written as:[35,49]

$$\phi(r) = \frac{A\exp\left[-\alpha\left(\frac{r}{r_e}-1\right)\right]}{1+\left(\frac{r}{r_e}-\kappa\right)^{20}} - \frac{B\exp\left[-\beta\left(\frac{r}{r_e}-1\right)\right]}{1+\left(\frac{r}{r_e}-\lambda\right)^{20}}. \tag{3.4}$$

F_i represents the embedding energy to embed an atom i into a local site with electron density ρ_i, which can be calculated using:[50]

$$\rho_i = \sum_{i=1}^{N} f_i(r_{ij}). \tag{3.5}$$

In the above expression, $f_j(r_{ij})$ represents the electron density at the site of atom i arising from atom j at a distance r_{ij} away. The functional form of the electron density is taken similar to the attractive term in the pair potential expression with same values of β and λ:[35]

$$f(r) = \frac{f_e\exp\left[-\beta\left(\frac{r}{r_e}-1\right)\right]}{1+\left(\frac{r}{r_e}-\lambda\right)^{20}} \tag{3.6}$$

The embedding energy functions F are chosen to work well over a wide range of electron density. For a smooth variation of the embedding energy, they are fitted to spline functions across different density ranges. The fitted parameters used in the embedded atom model are listed in Table II. For the oxygen-metal interactions, the potential parameters were fitted to reproduce the bulk properties of the respective oxides.[49]

B. MD simulation of metal oxidation

The minimum energy configurations obtained using the Monte Carlo simulations are first thermalized in the 0–300 K temperature range by cooling and heating in steps of 20 K. Each MD simulation comprised of 1000 equilibration steps ignoring the dynamic charge transfer between the metal atoms. The temperature was maintained constant at 300 K using a Nose-Hoover thermostat.[65] The surfaces are allowed to freely relax during these equilibration runs. The equilibrated samples are then simulated in a canonical, i.e., constant NVT ensemble (constant number of atoms, volume, and temperature) for 1 ps with dynamic charge transfer using the modified CTIP potential model to generate the final 300 K relaxed configuration. The atomic charges in the alloy metal samples were found to fluctuate around zero with a magnitude of $\pm 0.06e$ at the outermost layers and $\pm 0.02e$ in the bulk alloy. Similar charge fluctuation was observed in equilibrated pure Al samples by Hasnaoui *et al.*[29]

The oxidation of the metal substrates is initiated by introducing O_2 molecules in the vacuum slab at $x = 1.5r_c$ with their y and z positions chosen randomly (Fig. 2). The velocities of the O_2 molecules are chosen randomly from a Maxwell-Boltzmann distribution corresponding to the required temperature. Hence, the introduction of oxygen molecules does not bias the dynamics of oxidation. The initial component of the velocity along the x direction is chosen to

TABLE II. EAM parameters for metal-metal interaction (based on Zhou *et al.* Ref. 49).

Metal	r_e (Å)	F_e	ρ_e	ρ_s	α	β	A (eV)
Al	2.86392	1.20378	17.51747	19.90041	6.61317	3.52702	0.31487
Ni	2.48875	2.21149	30.37003	30.37137	8.38345	4.47117	0.42905

Metal	B(eV)	K	Λ	F_{n0}(eV)	F_{n1}(eV)	F_{n2}(eV)	F_{n3}(eV)
Al	0.36555	0.37985	0.75969	−2.80760	−0.30144	1.25856	−1.24760
Ni	0.63353	0.44360	0.82066	−2.69351	−0.07644	0.24144	−2.37563

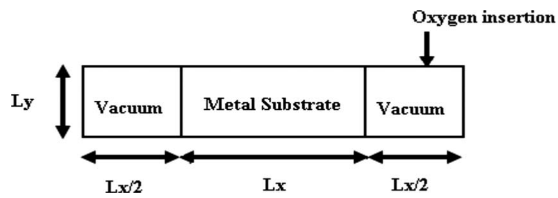

FIG. 2. Schematic showing the unit cell of alloy substrate and the vacuum slabs surrounding it. The box length along the z direction (L_z) is taken to be the same as that of the y direction (L_y). O_2 molecules are inserted at a distance equaling 1.5 times the cut-off radius of the potential function from the oxide layer.

have motion toward the metal substrate. Additionally, reflecting boundary conditions are imposed to the molecules that might reach the simulation box limit. The gas pressure is maintained constant during the simulation by introducing an O_2 molecule only when the previous molecule dissociates and forms bonds with the metal atoms. The equations of motion are integrated using a leapfrog scheme with time steps of 1 fs.[66] The charge relaxation procedure used to minimize the electrostatic energy subject to the electroneutrality principle is very time consuming. Hence, the atomic charges were updated every tenth MD step. The influence of a more frequent charge update was found to have no influence on the observed simulation results. The MD simulations were stopped when fragments of oxide species (AlO_4) are ejected into the gas phase owing to localized melting of the surfaces.

IV. RESULTS

A. Oxide growth kinetics

The kinetics of oxide growth on Ni-Al alloys of various compositions is presented in this section. Dynamic properties through the oxidation process and the effect of varying compositions of alloy substrate, as well as temperature and pressure, on the oxide growth characteristics are studied and discussed. Comparisons with oxide growth kinetics on pure Al and Ni substrate are also carried out.

1. Effect of alloy composition

Simulation of metal oxidation was performed for different compositions (0%, 5%, 10%, 15%, and 100% Ni) of Ni-Al alloy. The temperature during the entire oxidation process was maintained constant at 300 K. Figure 3 shows the total oxygen uptake as a function of the simulation time up to the limiting value of oxide thickness. For exposure times less than 75 ps, the kinetic curves obtained across different alloy compositions is similar. At longer simulation times beyond 75 ps, significant differences between the various substrate surfaces begin to show up. The total uptake of oxygen is found to decrease with increasing composition of Ni for the composition range simulated in this work. The oxide film thickness shown in Fig. 3(b) is defined as the distance between the x positions of the outermost aluminum atoms and the innermost oxygen atom in the simulated substrates. The oxidation of the surfaces reaches a limiting thickness, which corresponds to ~1.7, 1.4, 1.2, and 1.1 nm for 0%, 5%, 10%, and 15% Ni, respectively. For the range of temperature and gas pressures simulated in this work, we did not observe any noticeable nickel oxide formation and much longer simulation times are needed for the same, which are not amenable to the current MD simulations. Hence, the remaining sections mainly focus on the comparisons of Ni-Al oxidation kinetics and oxide growth on pure Al.

The oxidation kinetics on all the simulated surfaces obeys direct logarithmic growth kinetics except for the initial transient regime. This growth mode corresponds to the microscopic mechanism of oxide growth when ion movement results from extended defects. This is indeed the case for oxidation on Al surfaces.[29] The snapshots shown in Fig. 4 illustrate the oxidation process and the growth of oxide film on pure Al and 5% Ni alloy surfaces. It can be seen that the thickness of the oxide scale formed initially in the two cases is almost the same as seen from Figs. 4(a) and 4(b). However, at longer exposure times, the oxide scale formed on Al surface appears thicker than that observed in case of 5% Ni alloy surface. It is also interesting to note that while the growth process on Al surface appears to occur by a layer by layer mode, the growth front in the alloy surface reaches

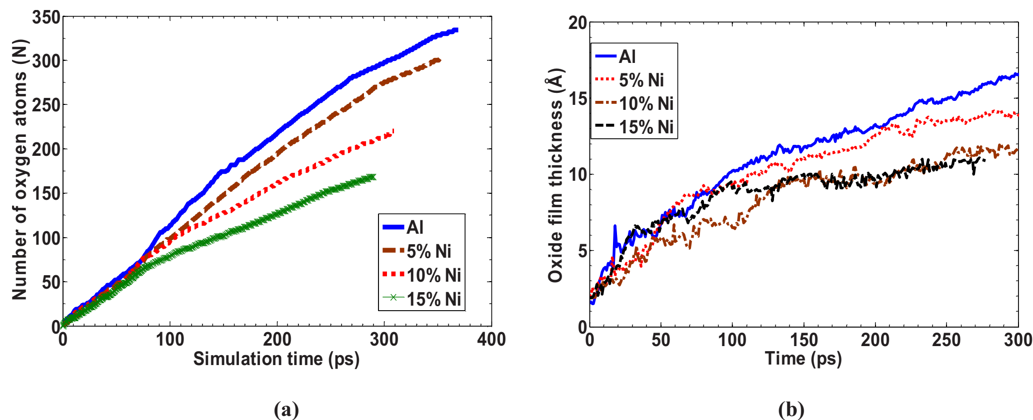

FIG. 3. (Color online) (a) Oxidation kinetics curves of Ni-Al alloy surfaces with varying composition of Ni. The curves represent the total uptake of oxygen as a function of the exposure time. (b) Variation of oxide film thickness with the exposure time for various compositions of Ni-Al surfaces.

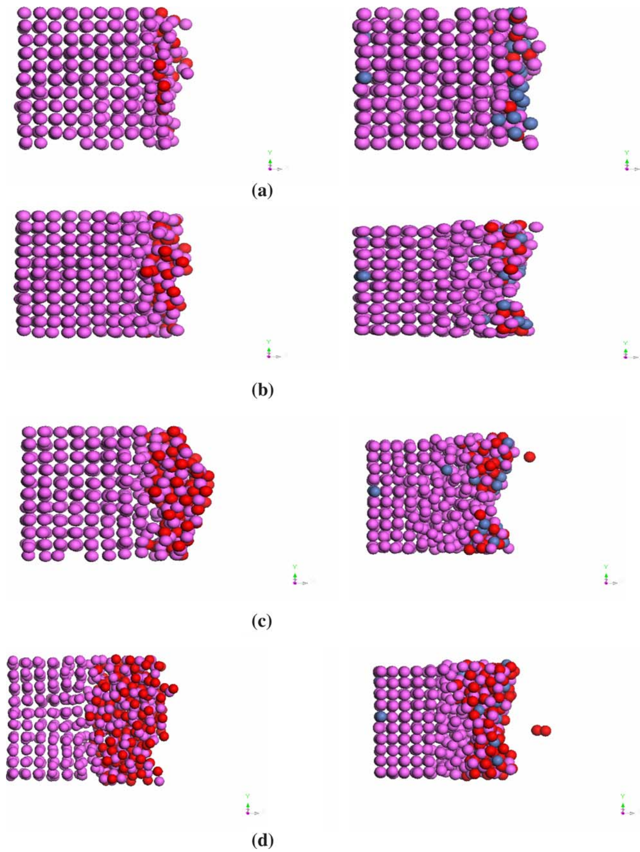

FIG. 4. (Color online) Snapshots showing the oxide growth on Al surface (shown on left-hand side) and 5% Ni-Al surface (shown on right-hand side) at various time instants (a) 15, (b) 50, (c) 75, and (d) 150 ps. Aluminum atoms are shown in pink, nickel atoms in blue, and oxygen atoms are shown in red.

second and third atomic layers before the first is completely oxidized [Figs. 4(a)–4(c)]. This result indicates that oxidation of alloy surfaces does not progress by the strict layer by layer process. The extent of deviation was found to increase with increasing Ni composition in Ni-Al alloy. Despite the differences in growth mode, the oxide structure formed on both the metal surfaces is amorphous in nature. The growth of the oxide film in the studied metal surfaces appears to result from the formation and movement of voids, which can be seen more clearly at the metal/metal oxide interface. This is in accordance with the theory of oxidation, which suggests the direct logarithmic growth to be associated with a growth mechanism where oxide film develops by ion migration via mobile voids in the amorphous oxide structure.[67]

2. Temperature effect

The effect of temperature on the oxidation kinetics was investigated by simulating pure Al and 5% Ni alloy surfaces at temperatures ranging from 300 to 500 K. The gas pressure was maintained constant at P_0. The rate of oxygen atom intake for the two surfaces is shown in Fig. 5. As expected, the kinetics of oxide growth becomes faster at higher temperatures. The oxidation kinetics at any given temperature exhibits an initial stage of fast oxide growth followed by low growth rate. Comparing Figs. 5(a) and 5(b), it can be seen that the oxygen uptake and therefore the oxide growth kinetics on pure Al surfaces is higher than those on 5% Ni alloy surface for the range of simulated temperatures. The difference in the rate of oxide growth between the two surfaces is found to increase with increasing temperature.

The theory of oxidation kinetics in ultrathin films can be utilized in conjunction with the simulation data derived from the oxidation kinetic curves shown in Fig. 5 to get an estimate of the activation energy barrier for oxidation on the two surfaces. The general expression for the potential (W) to be overcome in case of a field assisted migration of an ion between two adjacent sites is given as:[67]

$$W = W_0 - \frac{1}{2}qaE + \lambda L. \tag{4.1}$$

In the above equation, W_0 represents the intrinsic barrier for ionic jumps between two positions in the oxide film, q represents the charge on the ion, $2a$ represents the jump length, L is the oxide film thickness, and λ is a term that depends on the oxide structure. The second term on the right-hand side represents the lowering of the energy barrier by an electric field E across the oxide film, and the structure term (λ) represents structural changes in the oxide film associated with the film growth. One of the possible mechanisms for

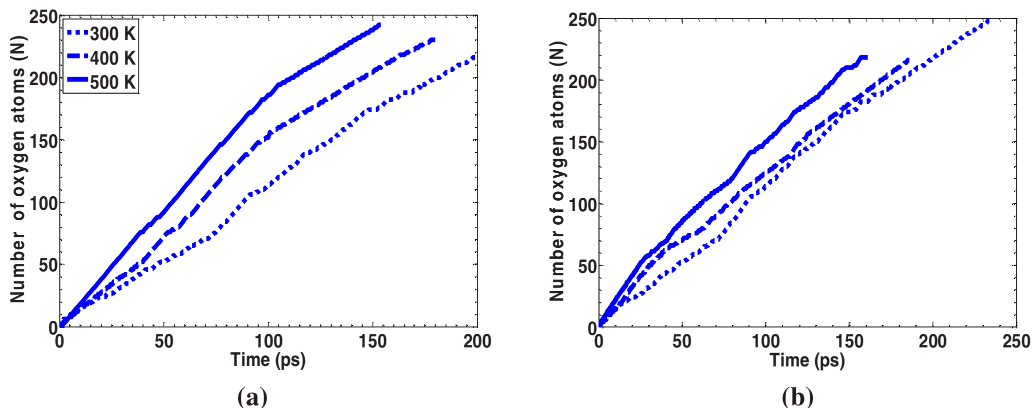

FIG. 5. (Color online) Oxidation kinetics curves of (a) Al and (b) 5% Ni-Al alloy surfaces at higher temperatures. The curves represent the total uptake of oxygen as a function of the exposure time.

oxide growth obeying direct logarithmic growth laws involves ion movement via extended defects or structural channels in the oxide layer. As the oxide film thickens, ion entry into the oxide is considered to become more difficult because of a closing or consolidation of these channels. The activation energy is therefore larger for thicker oxide films and the change is proportional to the oxide film thickness. The resulting rate equation is given by[67]

$$\frac{dL}{dt} = C \exp\left(-\frac{W_0 - \frac{1}{2}qaE + \lambda L}{k_B T}\right), \tag{4.2}$$

where k_B is the Boltzmann constant and C is a constant. The solution to the above equation yields a direct logarithmic growth law and is given by

$$L(t) = \left(\frac{k_B T}{\lambda}\right)\ln[1 + \mu(T)t]. \tag{4.3}$$

The term $\mu(T)$ is a temperature dependent term and is defined by

$$\mu(T) = \left(\frac{\lambda}{k_B T}\right) C \exp\left(-\frac{W_0 - \frac{1}{2}qaE}{k_B T}\right). \tag{4.4}$$

For large enough simulation times i.e., $\mu(T)t > 1$, Eq. (4.3) corresponds to a linear dependence of oxide thickness $L(t)$ on $\ln(t)$ as shown below;

$$L(t) = \left(\frac{k_B T}{\lambda}\right)\ln[\mu(T)] + \left(\frac{k_B T}{\lambda}\right)\ln(t). \tag{4.5}$$

Although it is possible to compute the average thickness of the oxide film at any given time instant as shown in Fig. 3(b), the statistical errors associated with such a computation make it more convenient to relate the total intake of oxygen atoms into the metal substrate to the oxide film thickness. For a homogeneous oxide, as is the case in the present study, the ratio of the oxygen intake $N(t)$ to the oxide film thickness is given by

$$\frac{N(t)}{L(t)} = A\rho, \tag{4.6}$$

where A represents the exposed surface area of the oxide film and ρ represents the density of the oxygen atoms in the oxide film. Equations (4.5) and (4.6) can be rewritten as

$$N(t) = \alpha \ln(t) + \beta. \tag{4.7}$$

Parameters α and β are defined by $\alpha = k'T/\lambda$ and $\beta = k'T/\lambda \ln[\mu(T)]$, where $k' = k_B A\rho$. In our simulations, the density ρ was found to be constant beyond 75 ps and did not vary with temperature. Hence k' can be considered as constant. After fitting the oxidation kinetic curves in Fig. 5 to Eq. (4.7), the estimates of the two parameters α and β can be obtained. Utilizing these two parameters, it is possible to estimate the structure term λ (in k' units) and $\mu(T)$. For example, the variation in structure term λ with temperature T is shown in Fig. 6 for the two surfaces. The structure term is a linear function of temperature and can be described by the following equations for pure Al and 5% Ni alloy surface, respectively:

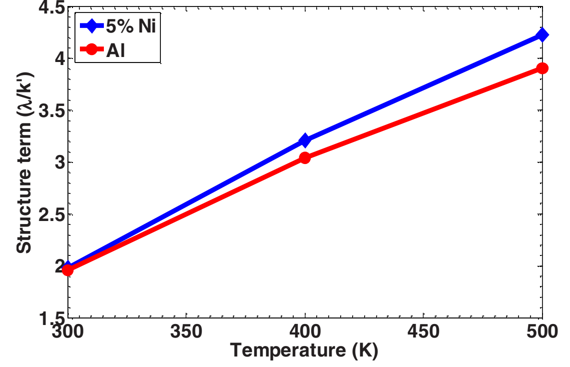

FIG. 6. (Color online) Variation of the structure term (λ) obtained by fitting the oxidation kinetic curves in Fig. 5 to Eq. (4.7).

$$\lambda = 9.70 \times 10^{-3}\ T - 0.92, \tag{4.8}$$

$$\lambda = 11.23 \times 10^{-3}\ T - 1.35. \tag{4.9}$$

It can be seen from Fig. 6 that the structure term λ is slightly higher for 5% Ni alloy surface in comparison to pure Al surface. Based on the activation energy defined by Eq. (4.1), increase in λ results in increasing the energy barrier required for oxidation. Hence, the increase in structure term results in reduced oxidation rates for the 5% Ni alloy surface. Similarly, the term $\mu(T)k'T/\lambda$ represents the Arrhenius dependence on the temperature as seen in Eq. (4.4). The fits of $\mu(T)k'T/\lambda$ term to the inverse of temperature allow us to deduce the following equation for pure Al and 5% Ni alloy surface:

$$C \exp\left(-\frac{W_0 - \frac{1}{2}qaE}{k_B T}\right) = \exp\left(\frac{-165}{T} - 7.39\right), \tag{4.10}$$

$$C \exp\left(-\frac{W_0 - \frac{1}{2}qaE}{k_B T}\right) = \exp\left(\frac{-176}{T} - 7.58\right). \tag{4.11}$$

Using these Arrhenius fits shown in Eqs. (4.10) and (4.11), it is possible to get an estimate of the term $W_0 - 1/2qaE$. We find this to be 0.014 and 0.015 eV for pure Al and 5% Ni alloy surface, respectively. If the value of the electric field E is known, then it is possible to get the exact estimate of the energy barrier W_0. Although it is not possible to estimate E using the current MD simulations, it can be obtained using published values of the electric field ($E \sim 7 \times 10^6$ V/cm).[13,33] In the present simulations, the average charge q of the oxygen atoms in the oxide film was found to be approximately $-1.86e$ and $-1.75e$ for Al and 5% Ni alloy surfaces, respectively. The oxygen jump distance can be approximated from the first peak distance in the pair distribution function for O-O (~2.9 and 3.3 Å for Al and 5% Ni-Al alloy, respectively). The field term $1/2qaE$ was found to be 0.38 and 0.40 eV, respectively. Thus, the activation energy barrier for Al and 5% Ni alloy surface is found to be 0.394

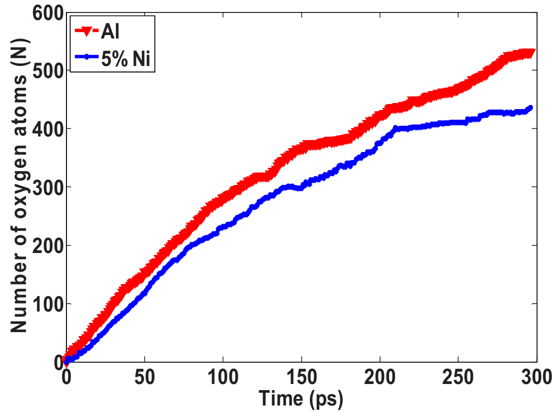

FIG. 7. (Color online) Oxidation kinetics curves of Al and 5% Ni-Al alloy surfaces at higher gas pressures ($3\times P_0$) and 300 K. The curves represent the total uptake of oxygen as a function of the exposure time.

and 0.415 eV, respectively. Statistically, the level of confidence used for this linear fit was 95%. The oxide formation in the alloy surfaces results from the oxidation of Al atoms, and Ni does not oxidize for the temperature range simulated. Hence, the small activation energy barrier difference between the two surfaces. There is no reported data on the activation energy barrier for oxidation on Ni-Al alloy surfaces. However, the activation energy barrier values for Al oxidation are available for comparison. The estimated activation energy barrier for pure Al is comparable to that estimated by Hasnaoui *et al.* ($\sim$0.39 eV) for Al oxidation in MD simulations utilizing Streitz-Mintmire potential function.

3. Effect of gas pressure

In order to investigate the dependency of oxide growth on the gas pressure, we simulated oxidation of Al and 5% Ni-Al surfaces at three P_0. The temperature is kept constant at 300 K. The kinetic curves showing the effect of gas pressure on oxide growth on Al and 5% Ni alloy metal surfaces are shown in Fig. 7. The oxidation kinetics is found to increase with increasing gas pressure for the two surfaces. At higher pressures also, the rate of oxide growth on Al surface is faster than on 5% Ni alloy surface. This can be explained by the increased supply of oxygen atoms at the Al/O interface. As also observed at higher temperatures, the kinetic curves show an initial fast oxide film growth followed by a slower oxide growth phase. Comparing Fig. 7 with Fig. 3(a), we find the differences in the growth rate kinetics between Al and 5% Ni alloy surface to increase with increasing oxygen pressures, especially at higher exposure times. Interestingly, we find that at these elevated gas pressures and 300 K, Ni also oxidizes. This was found to be true for higher oxygen exposure times.

B. Analysis of oxide structure

1. Pair distribution function

The pair distribution function (PDF) of the atoms in the oxide film as well as partial PDF of each type of atom was computed for 5% Ni-Al alloy substrate is shown in Fig. 8. In case of Al-Al pair distribution shown in Fig. 8(a), we observe a first peak around 2.9 Å, which corresponds to the first-nearest-neighbor distance in fcc Al lattice. Similar peak at 2.9 Å was also observed in case of Ni-Ni pair distribution as shown in Fig. 8(b). At early stages of oxide growth, we observed a second peak at $\sim$4 Å in Al-Al PDF, which corresponds to the second-nearest-neighbor distance. This peak subsequently disappears at higher exposure times when the oxide film is fully developed. The Al-O PDF [Fig. 8(c)] shows a peak at around 1.9 Å for exposure times beyond 25 ps i.e., the early oxide nucleation stage. This distance corresponds to the bond lengths reported in amorphous aluminum oxide, which ranges from 1.8–1.9 Å. On the other hand, the calculated Ni-O PDF for 5% Ni-Al alloy indicates an absence of a sharp peak and shows a distribution, which suggests the absence of formation of nickel oxide at low temperatures and pressure. The experimentally reported bond lengths of Ni-O by Caputi *et al.*[68] correspond to around 1.94 Å and hence any formation of nickel oxide should have resulted in a sharp peak in Ni-O PDF at that distance.

2. Analysis of atomic density profiles

The atomic density profiles at various stages of the oxidation process of Al and 5% Ni-Al alloy along the x axis i.e., perpendicular to the direction of oxide growth is shown in Fig. 9. Sharp peaks in the density distributions of both Al/O and Al/Ni/O systems are evident at lower exposure times i.e., less than 15 ps. At lower exposure times, which correspond to the early oxide nucleation stage, we find that the solidlike or crystalline lattice features are preserved as indicated by the distinct peaks shown in Figs. 9(a) and 9(b). With an increase in the oxygen exposure time and subsequent growth of the oxide film up to 75 ps, the peaks corresponding to the metal and oxide structures show lowering and broadening indicatives of greater atomic movement. For similar oxygen exposure times, we find that the lowering of peaks in the Al/O density profiles is greater than those in Al/Ni/O systems. The reduced lowering in alloy systems is attributed to decreased oxidation rates.

With an increase in exposure time, the outermost peaks exposed to the gas environment merge and become broader. For exposure times greater then 150 ps, the atomic distribution in the oxide phase becomes smooth indicative of the formation of an amorphous oxide structure. However, the bulk metal located at distance less than 10 Å is still crystalline, which is evident from the well defined inner peaks in the atomic density profile Figs. 9(a) and 9(b). The peaks at the oxide-metal interface in case of Al/O systems are lower and broader than the corresponding peaks in Al/Ni/O system. It can be clearly seen from the density profiles that the thickness of the oxide film formed in Al substrates in greater than that formed in 5% Ni-Al alloy system.

3. Charge distribution in alloy metal/metal oxide

The atomic charge distribution in case of Al and 5% Ni-Al substrate is shown in Fig. 10 as a function of x distance along the oxidation direction at 150 ps of exposure

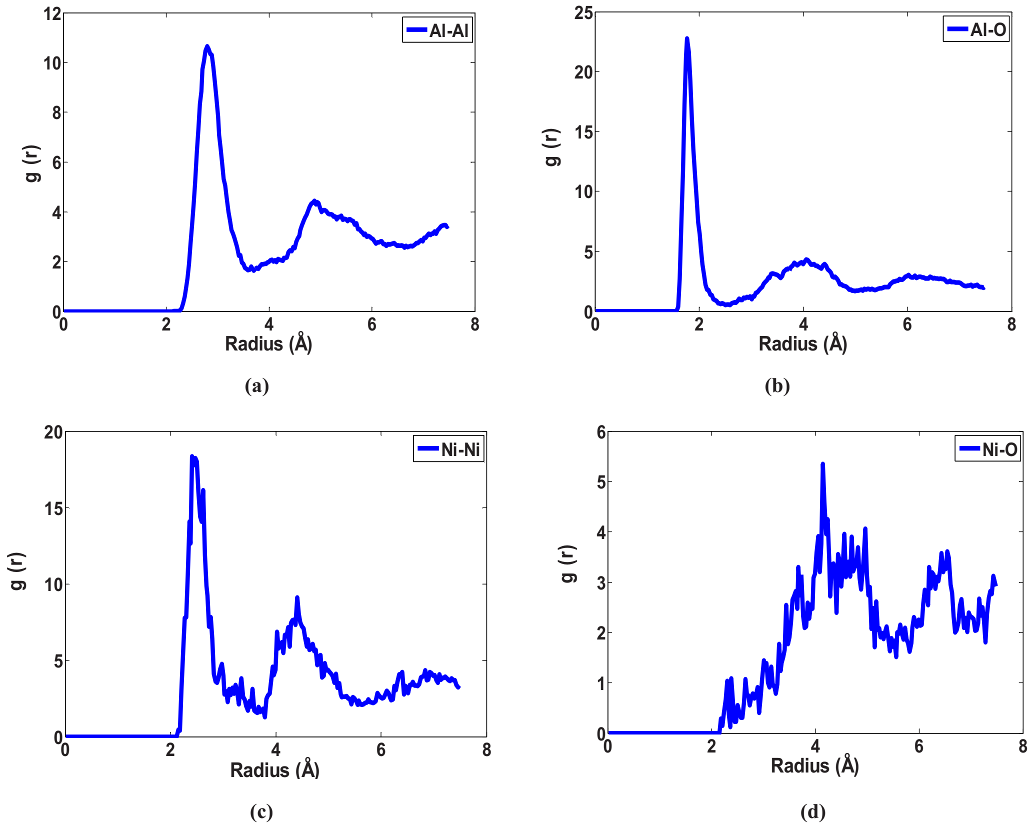

FIG. 8. (Color online) Pair distribution function (a) Al-Al, (b) Ni-Ni, (c) Al-O, and (d) Ni-O in Al/Ni/O system taken at 150 ps of exposure time. The calculated bond lengths are summarized in Table IV.

time for (100) surface. It can be clearly seen that the atomic charges in the bulk metal substrates in both cases present charges, which fluctuate around zero value. The positive charges in the oxide film are due to metal atoms i.e., aluminum and nickel, whereas the negative charge is attributed to the oxygen atoms. Upon checking for the zero charge condition for the charge distributions in both the cases, we find that the fluctuations around zero value reached a maximum of 0.25*e* at the gas/oxide interface and 0.12*e* in the oxide interior.

The oxygen atoms are weakly charged close to the oxide-gas interface and decrease to higher negative values in the oxide interior. The values reach a maximum negative value at approximately 0.7 and 0.5 nm, respectively from the oxide-gas interface for Al/O and Al/Ni/O systems. The charges on oxygen atoms then decrease to lesser negative values close to the metal oxide interface. The reduction in the magnitude of the oxygen charges near the oxide-gas interface is attributed to the insufficient concentrations of cations to ionize the oxygen in the oxygen rich surface region. Additionally, the oxygen charge close to the metal-oxide interface is also low since they are ionized by cations, which are weakly charged. Thus the charge distribution in the metal oxide film is not homogeneous and is strongly correlated

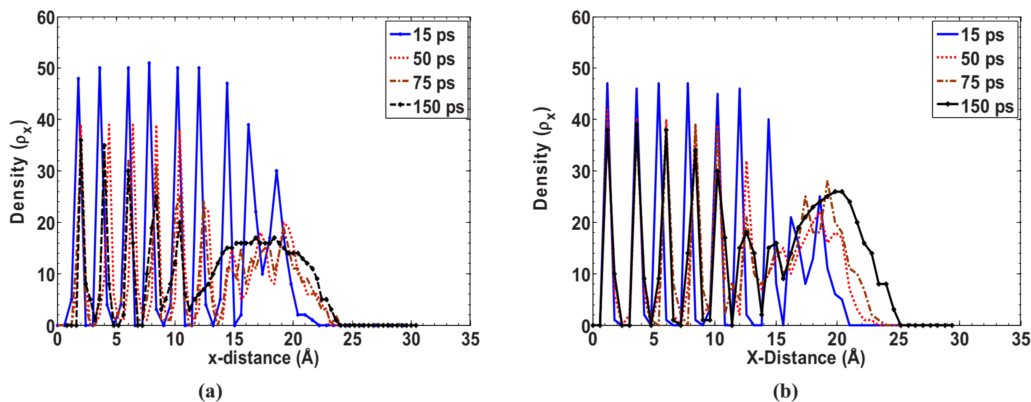

FIG. 9. (Color online) Atomic density distribution in (a) Al/O and (b) Al/Ni/O systems taken at 15, 50, 75, and 150 ps of exposure time. The density distribution is shown as number density of atoms along the x direction in the sample.

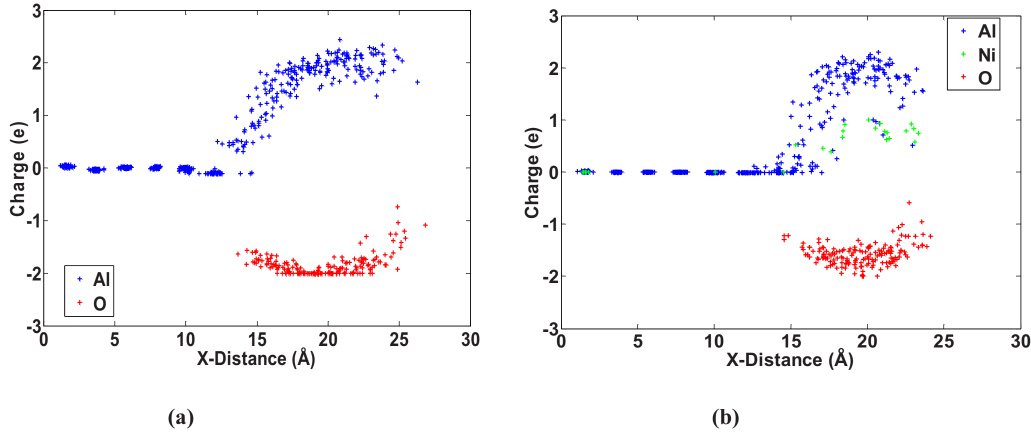

FIG. 10. (Color online) Charge distribution in (a) Al/O and (b) Al/Ni/O systems (5% Ni) taken at 150 ps of exposure time. The charge distribution is shown as charge of each atom in e units ($e=1.6\times10^{-19}$ C) versus its x position in the sample.

with the coordination number (in terms of neighboring oxygen atoms) of the metal atoms. We find that the charges of the Al atoms increase with an increase in their coordination numbers. Details about the evolution of the Al coordination numbers and the mechanism of nanoscale oxide growth are discussed in the next section.

C. Mechanism of nanoscale oxide growth

The atomistic mechanism of nanoscale oxide growth is investigated by analyzing the time evolution of Al coordination in the oxide film as well as monitoring the diffusion of metal and oxygen atoms at the oxide-metal and gas-metal interfaces. The progression of the oxide layers at the two interfaces in case of Al and Al/Ni systems is compared with gain insights into the differing growth kinetics in the two systems.

1. Time evolution of Al coordination in oxide structures

The distribution of Al-O coordination numbers in the oxide film can be characterized in terms of the frequencies of various atomic configurations such as $Z=3$, 4, 5, and 6. Based on the calculated bond lengths using PDF, we calculated the average coordination number of Al-O in the oxide film as it develops during the oxidation process. The results shown in Fig. 11 and Table III were determined from atomic trajectories using a spherical radius $R=1.2r_0$, where r_0 represents the first-nearest-neighbor distance obtained in the PDF curve for Al-O. The values were obtained by averaging over time beyond 200 ps of exposure time.

Based on the distribution of coordination numbers [shown in Fig. 11(a)], the initial stage of oxide growth is dominated by the presence of $Z(\text{Al}-\text{O})=4$. For exposure times less than 100 ps, the coordination $Z(\text{Al}-\text{O})=4$ was found to be present at approximately 70% of the oxide scale. For exposure times greater than 100 ps, we find that $Z(\text{Al}-\text{O})=6$ starts to build up and begins to contribute to the formation of oxide structure. This suggests that for Al-O system, during the initial oxide growth phase, AlO_4 tetrahedron plays an important role in building up the amorphous oxide film structure. As the oxide film develops, it becomes more heterogeneous. Our calculations based on Al coordination numbers and bond angle distribution calculated for various shells across the oxide film indicate a gradual change from $Z=4$ near the metal-oxide interface to $Z=6$ near the gas-oxide

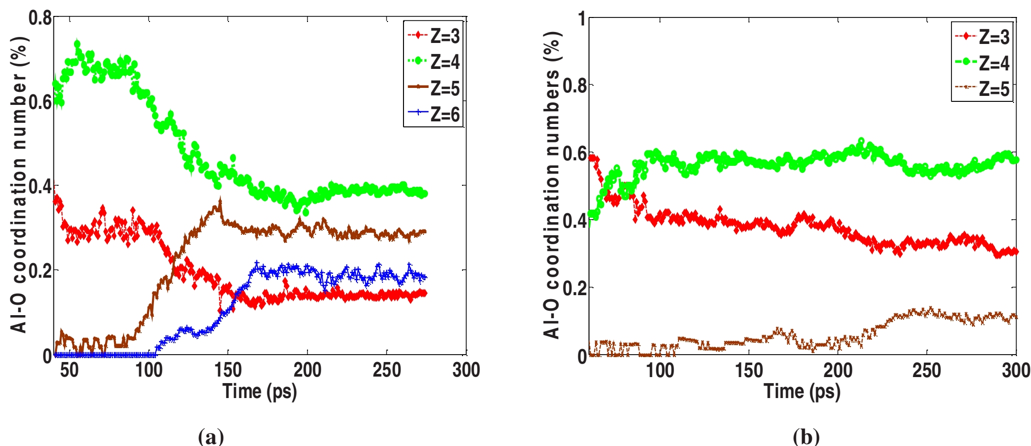

FIG. 11. (Color online) Time evolution of the different coordination numbers ($Z=3$, 4, and 5) of Al-O bond in the (a) Al/O and (b) Al/Ni/O systems.

TABLE III. Distribution of Al-O coordination numbers in Al/O and Al/Ni/O systems. The simulated values represent averages taken beyond 200 ps of exposure time.

Z	% atoms (Al-O system)	% atoms (Al/Ni/O system with 5% Ni)
3	14	33
4	39	57
5	29	10
6	19	<1%

interface suggestive of a mixed tetrahedral and octahedral environment. Such a variation in Al coordination numbers was also observed in the oxidation simulations by Hasnaoui *et al.*[28] and Campbell *et al.*[31,32] The oxide configurations beyond 150 ps of exposure time have average (Al-O) coordination numbers: $Z(\mathrm{Al-O})=3$ (14%), 4 (39%), 5 (29%), and 6 (19%).

In case of Ni-Al alloy systems, our simulation results suggest that the initial growth of oxide film results from the build up of AlO_4 fragments. However, in contrast to Al systems, we find an absence of AlO_6 configuration in 5% Ni-Al as shown in Fig. 11(b). Additionally, the fraction of five coordinated Al atoms is also much lower than that observed in pure Al systems. Thus the structure of the alloy oxide film presents a dominant tetrahedral environment in the inner and outer layers for exposure times greater than 150 ps. Similar behavior was also observed at higher Ni compositions. The oxide configurations beyond 150 ps of exposure time for 5% Ni-Al system have an average (Al-O) coordination numbers: $Z(\mathrm{Al-O})=3$ (33%), 4 (57%), and 5(10%). Thus, the oxide structure obtained in case of alloy surfaces is very different from those observed in single metal constituents. It appears that the faster kinetics associated with Al oxidation results in the mixed tetrahedral and octahedral environment, whereas the relatively slower kinetics associated with alloy surfaces gives rise to predominantly tetrahedral environment. Thus, the oxidation kinetics is strongly correlated with the morphology and structure of the oxide film.

2. Mean-square displacement and diffusion coefficients

The oxide growth characteristics of the metal surfaces were explored using shell based diffusion coefficients. The shell based diffusion coefficients allow for comparison of early stages of oxide growth in pure Al substrate with that of Ni-Al surface. In the case of pure Al and Ni-Al alloy surfaces, we find that the oxide growth proceeds via inward movement of oxygen anions (metal-oxide/gas interface) and outward movement of metal cations (metal/metal-oxide interface). Partitioning the metal-oxide structure into different shells of equal width (dR) allows for estimating the atomic mobility located at the oxide interior as well as at the two interfaces. The mean-square displacement (MSD) (Ref. 69) calculated within each shell was used to obtain the self-diffusion coefficient using Eq. (4.12) for atoms in that shell.

$$D_i = \frac{1}{2d\Delta t}\langle |r_i(t+s) - r_i(s)|^2 \rangle, \qquad (4.12)$$

where $\mathbf{r}_i(t+s)$ is the vector position of the ith atom, the average is over atoms of type i and over choices of time origin s. The average interatomic distance between atoms was used as dR. The MSD for each shell was generated by averaging over a 1 ps trajectory sampling every 1 fs. The one-dimensional diffusion coefficient is calculated using above reflects the mobility of the atoms along the x axis, which corresponds to the direction of oxide growth and characterizes the out-of-plane movement. Similarly, the in-plane movement refers to mobility of the atoms in the shells perpendicular to the growth direction (z direction) and is the two-dimensional (2D) ($d=2$) diffusion coefficient calculated based on the $\mathbf{y}$ and $\mathbf{z}$ position vectors of atoms i.e., on the y-z plane (cross section). These in-plane and out-of-plane diffusion coefficients calculated based on MSD were assigned to each shell. To facilitate comparisons between the pure Al and Ni-Al alloy surfaces, diffusion coefficients calculated for the same shells and their dependence on $\mathbf{x}$ distance has been plotted.

Our analysis of the density profiles indicates that there is both an inward and outward growths of the oxide scale in pure Al as well as alloy surfaces. The inward growth results from the diffusion of the oxygen atoms, whereas the outward growth is attributed to the diffusion of metal atoms. The MSD of oxygen and metal atoms located at the metal-oxide and oxide-gas interfaces for the two surfaces are shown in Fig. 12. It can be seen that the inward movement of oxygen atoms exceeds the outward movement of metal atoms and is primarily responsible for the growth of the oxide scale in both the surfaces. This is in agreement with the experimental observations of oxidation studies conducted on Al surfaces.[70] However, the extent of inward to outward diffusion of the atoms is different in case of pure Al and Ni-Al alloy surfaces having 5% Ni. In both Al and Ni-Al surfaces, the outward diffusion of the metal atoms calculated at times greater than 100 ps is similar, whereas the inward diffusion of oxygen atoms is lower for Ni-Al compared to Al surface. Therefore, the limiting thickness of the oxide scale formed in case of Ni-Al alloys is lower compared to that in pure Al. The limiting thickness was found to decrease with increasing composition of Ni and resulted from reduced inward growth of the oxide scale.

The large stress gradients that are associated with the oxidation process give rise to diffusion of atoms in the oxide region. Additional insights into the same as well as their role in the growth of the oxide scale can be obtained using the shell based diffusion coefficients shown in Fig. 13, which are calculated at various exposure times for the two surfaces. Typical atomic diffusivities in the oxide film are in the range of $1.5-2.7\times10^{-6}$ cm^2/s for Al and $1.1-2.2\times10^{-6}$ cm^2/s for 5% Ni-Al surfaces, respectively. It can be seen that initial oxidation of both the pure Al and 5% Ni-Al alloy surfaces is associated with increased diffusivities of atoms that are located at the outermost shells around 20 Å. Initially for shorter exposure times less than 15 ps, the diffusivities of atoms located on the outermost shell i.e., shell seven are

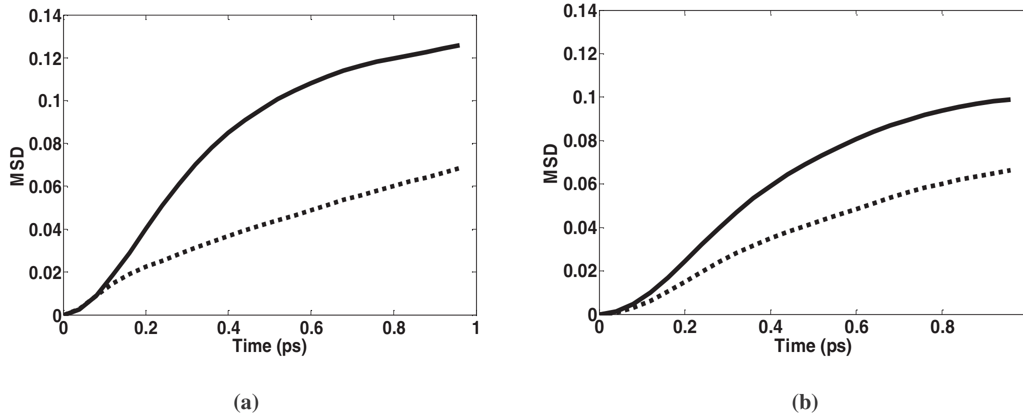

FIG. 12. MSD representing the inward diffusion of oxygen atoms (solid line) and the outward diffusion of metal atoms (dashed line) located at the oxide-gas and metal-oxide interfaces, respectively, for (a) Al and (b) Ni-Al surfaces having 5% Ni. MSD shown is at 100 ps of exposure time. The inward diffusion of anions exceeds the outward diffusion of cations and is predominantly responsible for oxide growth in both the systems.

much higher than the remaining shells. As the oxidation proceeds to higher times, atoms in the outer shells such as six also show much higher diffusivity characteristic of amorphous oxide phase, whereas those in the first three remain solidlike as seen in bulk metals. At exposure times greater than 100 ps, shell four and five also exhibits similar behavior.

Comparison of the shell based diffusion coefficients in Fig. 13 with the atomic density profiles shown in Fig. 9 indicates that the maximum in shell based diffusion coefficients corresponds to the metal-oxide interface. The diffusivities of atoms located at the outermost shell, which corresponds to the oxide-gas interface, are lower than those of the atoms at the metal-oxide interface. Additionally, the calculated shell based diffusion coefficients, especially at the metal-oxide interface are higher for Al oxidation than for 5% Ni-Al alloy surface. In both the cases, we find that with increasing exposure time, there is a progressive shift in the maxima toward the substrate interior, which corresponds to the inward growth of the oxide. Correspondingly, there is also an outward growth of the oxide as indicated by increased diffusivities of shell seven at 15 ps to shells eight and 9 nine at longer exposure times. The extent of inward oxide growth is higher than the outward. Additionally comparing Figs. 13(a) and 13(b) indicates that while the outward growth of the oxide in both Al and Ni-Al surfaces is similar, inward growth of the oxide in case of Al substrate is larger than in 5% Ni alloy substrate.

Similarly, we have also analyzed the in-plane diffusivities of the atoms in the various shells. Across different shells in the oxide film, we do not observe a significant difference in the in-plane atomic diffusivities, especially for exposure times greater than 75 ps. Our analysis of Al and O diffusivities in the various shells located in the oxide interior for exposure time less than 100 ps indicates 40%–70% higher diffusivities of metal atoms in comparison with oxygen atoms, which are attributed to the smaller steric size of aluminum. For example, in case of pure Al, the O and Al diffusivities at 75 ps were found to be 3.5×10^{-6} and 5.7×10^{-6} cm^2/s, respectively. Similarly, in case of 5% Ni-Al alloy, the O, Ni, and Al diffusivities at 75 ps were found to be 4.9×10^{-6}, 4.0×10^{-6}, and 6.9×10^{-6} cm^2/s, respectively. At higher exposure times, the diffusivities of metal atoms decrease, whereas that of oxygen atoms remains somewhat

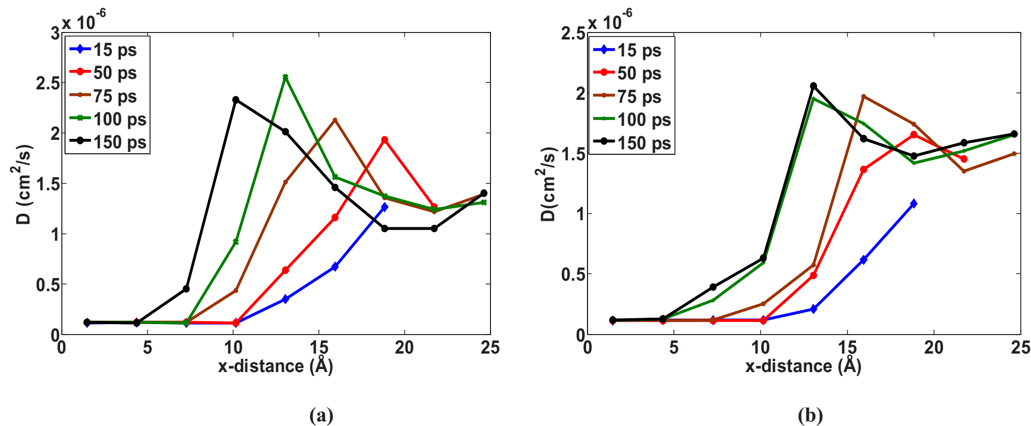

FIG. 13. (Color online) Shell based diffusion coefficients showing the oxide growth in (a) Al and (b) 5% Ni-Al surfaces. The mobility of ions resulting in the inward and outward growths of the oxide film on the two surfaces is shown as function of simulation time.

constant. For 5% Ni-Al alloy, the O, Ni, and Al diffusivities at 150 ps were found to be 4.5×10^{-6}, 3.5×10^{-6}, and 5.4×10^{-6} cm^2/s, respectively.

Initially for exposure time less than 75 ps in case of 5% Ni-Al alloy, we observe that the out-of-plane diffusion coefficients is higher than the in-plane diffusion coefficient. During this time, the O atoms are able to penetrate into the sublayer of the substrate and bond with the Al atoms that are present in the second and third atomic layer. The oxidation of alloy surfaces thus creates 2D oxide islands in an atomic layer, while the metal islands exist in the previous atomic layer. This suggests that the initial oxidation of alloy surfaces does not progress by the strict layer by layer process. At longer exposure times i.e., above 100 ps, the in-plane diffusion coefficients calculated across the shells in the oxide interior are 30%–40% higher than the out-of-plane diffusion. The higher in-plane diffusion ensures that the 2D oxide growth in a particular atomic layer is completed before the growth front can proceed to the next atomic layer. This marks a transition from the initial island growth mode to a layer by layer growth mode. In contrast, the in-plane diffusion coefficients calculated for the oxide scale formed on pure Al is higher than out-of-plane diffusion coefficient throughout the oxidation process. Thus in case of pure Al, the growth and development of the oxide film proceeds in a layer by layer mode at all stages.

V. DISCUSSION

Our simulations of pure Ni surfaces at 300 K and pressure$=9.8\times10^5$ Pa indicate that the oxidation kinetics is significantly slower than those observed for Al and Al alloy surfaces. For exposure times up to 300 ps, the uptake of oxygen was less than 20 atoms. This observation is in accordance with previous experimental investigations of oxidation on Ni surfaces, which suggest that for oxygen coverages below 0.5 monolayers and temperatures below 550 K, oxygen remains in two-dimensional chemisorbed state without any detectable formation of nickel oxide or dissolution of oxygen into the metal lattice.[71]

Ab initio studies of oxygen adsorption on Ni-Al surfaces indicate the preference of O atoms to have Al as a neighbor rather than Ni.[47] The presence of O atom on a Ni-Ni bridge site was found to push the Ni atoms away, while the neighboring Al atoms moved toward it. Previous *ab initio*, as well as experimental investigations, doubts the possibility of Ni-O bond formation in low-temperature oxide and does not rule out the presence of metallic Ni in the oxide scale.[72] In this work, we find that the oxide structure for various simulated alloy compositions is predominantly composed of aluminum oxide. Hence, the oxidation of nickel is significantly reduced in comparison with aluminum. For increasing composition of Ni in the Ni-Al alloy, the layers close to the exposed metal surface have higher compositions of Ni. Hence the surface sites available for oxidation reduce with increasing Ni composition in the Ni-Al alloy. During the initial phase of oxidation, the oxygen molecules for varying alloy compositions have enough Al surface sites for oxidation. However, with increasing composition of Ni, especially at longer simulation times, the oxygen diffusion into the substrate is impeded. This results in the reduced oxidation rates at higher Ni compositions. The onset of the low growth rate regime therefore occurs at earlier exposure times for increasing Ni compositions. The reduced oxidation rate and hence the oxygen intake results in accumulation of oxygen atoms at the substrate surface leading to surface melting. The simulations of oxide growth kinetics were stopped once we observe ejection of oxide fragments from the metal surface.

It should be noted that the ejection of AlO_4 fragments is not dependent on the introduction of oxygen molecules into the system. The ejection of AlO_4 fragments was observed in case of Al nanocluster oxidation by Campbell *et al.*[31,32] for simulation times longer than 50 ps in both canonical and microcanonical ensembles. Hasnaoui *et al.*[28,29] also observed a similar process in their oxidation study of Al substrates. While Hasnaoui *et al.* introduced oxygen molecules one by one to study the kinetics of oxidation on Al surfaces, Campbell *et al.* performed their simulations with much higher number densities of randomly distributed oxygen molecules. In the present work, despite the use of the Nose-Hoover thermostat to dissipate heat, we observe that beyond 200–300 ps of simulation time, the oxide structure starts melting at the surface region. This is attributed to the accumulation of dissociated oxygen at the metal surface upon reaching the limiting regime when their intake into the substrate is impeded. Experimental observation of oxide growth kinetic curves until the saturation regime is reached when growth rates tend to nearly vanish; is possible at low temperature. However, such a regime requires much longer simulation times (several hundred seconds), which are not accessible to MD simulations. Therefore, the rate curves presented in the current study are obtained until the oxide growth reaches a low growth rate regime termed as limiting regime. The limiting thickness of the oxide film corresponds to the oxide scale formed in this low growth rate regime.

The limiting thickness of the oxide scale formed is smaller for increased Ni composition. This can be seen in Fig. 3(b), which shows the oxide film thickness variation with exposure times for the various simulated alloy compositions. The oxidation of the simulated metal surfaces reaches a limiting thickness, which range from 1.7–1.1 nm for 0%–15% Ni. These values are in good agreement with the experimental studies of Lamparter *et al.*[14] who found the thickness of aluminum oxide scales to reach ~1.5 nm. Similarly, Gaßmann *et al.*,[48] and Isern and Castro,[45] as well as Yoshitake *et al.*,[73] observed a 5 Å thick scale to form on 50% Ni-Al alloy surface which is very close to the extrapolated self-limiting thickness (3.2 Å) predicted using the current MD simulations.

The structure of the oxide scale formed in our simulations can be compared with those reported in previous experimental and theoretical studies. The comparisons of the calculated bond lengths in this work and those reported previously are presented in Table IV. We find good qualitative and quantitative agreement with the previously reported experimental and simulation studies. Comparison of Al-O and Ni-O PDF at various stages of oxidation at 300 K and pressure P_0 indicates that the oxide film formation and growth in case of 5% Ni-Al alloy is attributed entirely to oxidation of alumi-

TABLE IV. Comparison of calculated bond lengths (R_{ij}) in this work with those reported in previous theoretical and experimental investigation of Ni-Al and Al oxidation, respectively. The bond lengths listed in the present work are for oxide scale formed on 5% Ni-Al alloy.

Bond lengths	Present work (MD simulations) R_{ij}(Å)	Finnis *et al.*[a,b] (*ab initio* simulations) R_{ij}(Å)	Stierle *et al.*[c] (Experimental) R_{ij}(Å)	Lamparter and Kniep[d] (Experimental) R_{ij}(Å)
Al-Al	2.9	2.9		3.2
Al-O	1.9	1.79	1.9	1.8
O-O	3.3		3.0	2.8
Ni-O	Absent		Absent	

[a]Reference 50.
[b]Reference 72.
[c]Reference 74.
[d]Reference 14.

num atoms. At low temperatures and pressure, we observed similar behavior across the range of alloy composition investigated. Under these conditions, the observed decrease in the rate of oxidation with increasing composition of Ni appears to result primarily from the reduced number of surface sites that are available for oxidation. These findings are in agreement with previous experimental investigations of initial oxidation on Ni-Al (110) surface by Isern and Castro,[45] which also indicate the lack of nickel-oxygen interaction. The oxide scale was composed entirely of Al_2O_3 and oxygen uptake stops after formation of a thin layer of Al_2O_3, which prevents further oxygen transport into the bulk. Similar observations were also made by Franchy *et al.*[75] and Jaeger *et al.*[46] in their experimental studies of oxygen adsorption on Ni-Al(111) surfaces at low temperatures.

The charge distribution profiles obtained for the oxide scale formed in the two systems corroborate the above findings. In case of Al/Ni/O system, it can be seen that Ni atoms are weakly charged and do not assume full valence values. The charge transfer appears to take place primarily between the O atom and the nearest Al atoms. Although some charge appears to have been transferred from the nearest Ni atoms to O atom as seen from Fig. 10, our analysis indicates that the charge values of Ni atom in the oxide interior fluctuates between 0 and $+1e$. This seems to suggest that there appears to be a tendency on the part of Ni atoms to form oxide. However, the bond formed between oxygen and Ni does not appear to be stable. It is possible that the Ni-O bond formed is quickly replaced by the more stable Al-O bond. The CTIP-EAM model used in the current work is able to account for this bond formation and bond breakage phenomena occurring in metal/metal-oxide systems. Furthermore, this argument is also supported by thermodynamic considerations. If we compare the enthalpy of formation of the respective oxides, $H_f(\mathrm{NiO})=-489.5$ kJ/mol and $H_f(\mathrm{Al_2O_3})=-1675.7$ kJ/mol, it can be seen that it is more favorable to form Al-O bond.[72,76] This manifests itself in the form of lack of nickel oxide formation shown in the pair distribution calculated by averaging over many such configurations. This is also in excellent agreement with the findings of Bardi *et al.*,[77] who studied the initial oxidation of Ni-Al alloy and analyzed the aluminum oxide overlayer by x-ray photoemission spectroscopy (XPS), low-energy ion scattering (LEIS), and low-energy electron diffraction (LEED). On the other hand, in the oxide interior Al atoms forming oxide attain charge values close their full valence charge. This suggests that the oxide formed is almost entirely due to oxidation of aluminum atoms and corroborates the findings obtained using PDF. In both the systems, the cations are weakly charged close to the metal-oxide interface and assume charges greater than $2.2e$ in the oxide interior. A small decrease in the Al atom charge at the oxide environment is observed in case of Al/O systems, whereas a significant decrease to around $1e$ is observed in case of Al/Ni/O system. The weakly charged Al atoms at the oxide-environment interface in case of alloy systems might also result in reduced oxidation rates.

Our analysis of the oxide structure indicates that the aluminum oxide scale formed on the alloy surface is different from that formed on the pure Al substrates. It is interesting to note the difference in oxide structure between the two cases even though 5% Ni-Al system has a small number of Ni atoms. This is attributed to the surface segregation of low content alloys, which results in Ni atoms occupying more surface sites than would be expected if the atoms were distributed uniformly across the metal substrate. For a 5% Ni-Al alloy, the exposed metal substrate thus has nearly 35% of the surface sites occupied by Ni atoms. Hence, the fraction of Ni atoms in the growing oxide film is significantly larger even for a 5% alloy. The existence of differences in the structure of the oxide film formed on Pure Al and Ni-Al alloy substrates was also observed in the *ab initio* studies by Jennison and co-workers,[78,79] and Kresse *et al.*[80] for ultrathin aluminum oxide scale formed on Ni-Al alloy surfaces. First-principles density-functional calculations by Jennison *et al.*[79] on the structure of ultrathin films (with self-limiting thickness less than 20 Å) on Ni-Al surfaces predicted a different Al_2O_3 structure, which has no bulk counterpart. As observed in our simulations, it was reported that the Al ions prefer distorted tetrahedral sites over the normal octahedral sites. The experimental studies on ultrathin aluminum oxide film formed on Ni-Al(110) by Stierle and co-workers,[81,82] and Gassmann *et al.*[83] also support this conclusion. Similar con-

clusions were drawn from the atomistic information gained by scanning tunneling microscopy (STM) with *ab initio* density-functional theory (DFT) by Kresse *et al.*[80] Our simulation findings also agree fairly well with the high-resolution photoemission study of nanoscale aluminum oxide films on Ni-Al (110) formed at room temperature, which was found to comprise of predominately (90%) tetrahedral coordinated Al.[84] On the other hand, the first-principles investigation of oxide structure formed on pure Al substrates by Jennison and Bogicevic[85,86] indicated that the lowest-energy stable film has an even mix of tetrahedral and octahedral site Al ions, and thus most closely resembles the *Ic* phase of bulk alumina. This is in good agreement with the distribution reported in the current simulations.

VI. CONCLUSION

The oxidation kinetics of Ni-Al alloy surfaces have been studied using MD simulations. The effect of temperature (300–500 K), oxygen gas pressure ($9.8\times10^5-2.9\times10^6$ Pa) as well as alloy composition (0%–15% Ni) on the kinetics of oxidation was investigated. In the simulated temperature-pressure regime for Ni-Al alloys of varying composition, we find that the oxide growth curves follow a direct logarithmic law beyond an initial transient regime. For a given alloy composition, the oxidation rate increases with temperature and pressure. In the simulated composition range (0%–15% Ni), the oxidation rates for Ni-Al alloys were found to decrease with increasing Ni composition. The oxidation kinetics of pure Ni was much slower than that observed in pure Al and Ni-Al alloys. Investigation of the temperature and gas pressure effect on the oxidation kinetics suggests an increasing difference in the rate of oxide growth between pure Al and 5% Ni-Al alloy surfaces with temperature and pressure. The activation energy barriers for oxidation on pure Al and 5% Ni-Al surfaces were calculated by fitting the growth law to the simulated kinetic curves. We find that the activation energy barrier for 5% N-Al alloy ($\sim$0.42 eV) to be slightly higher than those observed for pure Al surfaces ($\sim$0.39 eV).

Structural and dynamical correlation functions were also used to identify the morphological evolution and growth of the oxide scale formed on various metal surfaces. At low temperatures and pressures, the analysis of structural correlation functions indicates that the oxide scales formed on Al-Ni result entirely from oxidation of Al. Ni was found to form a negligible portion of oxide except at higher pressures when the oxidation kinetics of Ni is expected to be faster. Oxide films formed on the various simulated metal surfaces are amorphous in nature and have a limiting thickness ranging from $\sim$1.7 nm for pure Al to 1.1 nm for 15% Ni-Al surface. The limiting thickness of the oxide scale thus decreases with increasing composition of Ni in the composition range simulated. We also find that the oxide scales formed on pure Al surfaces have a dominant tetrahedral (AlO_4) environment in the oxide interior and mixed tetrahedral (39%) and octahedral modes ($\sim$19%) at the oxide-gas and metal-oxide interfaces. On the other hand, the oxide scales formed on the alloy surfaces is almost entirely composed of (AlO_4) fragments ($\sim$60%). The octahedral environment (AlO_6) was absent in alloy surfaces ($<1\%$). The analysis of the amorphous structure formed is in agreement with previously reported experimental and theoretical studies. The differences in the structures of the alloy and single metal oxides suggest strong correlation of the morphology with kinetics of oxidation. In all the simulations, significant charge transfer was observed in the reactive region i.e., oxide scale.

Atomistic observation of the growth process and analysis of the dynamical correlation functions suggests a layer by layer growth on pure Al surfaces. Deviations from the layer by layer growth mode were observed for 5% Ni-Al alloy surfaces during the initial oxidation stage when growth proceeds by island growth mode. Shell based diffusion coefficients were used to identify the diffusion mechanism that leads to the oxide formation and growth on these metal surfaces. For both pure Al and 5% Ni alloy surfaces, we find that the growth proceeds via inward oxygen migration and outward metal ion migration. The extent of outward growth in both cases was found to be the same. However, the inward growth resulting from oxygen migration was reduced in the case of 5% Ni alloy surfaces when compared to pure Al. This was found to be responsible for the reduced limiting oxide thickness with increasing compositions of Ni in the Ni-Al alloy. The findings of the current research agree well with previous experimental investigations and provide useful insights into the oxidation mechanism and nanoscale oxide growth on Ni-Al alloy surfaces.

ACKNOWLEDGMENTS

The authors gratefully acknowledge the computational facilities provided by the research computing core at University of South Florida and CNS-NNIN at Harvard University. The authors also thank Julian Gale for providing the molecular dynamics code GULP 3.1 and Will Smith for providing DL_POLY 2.14, which are modified and used in the current research. The financial support from the Office of Naval Research is gratefully acknowledged.

*Corresponding author. shriram@deas.harvard.edu.

[1] H. Over and A. P. Seitsonen, Science **297**, 2003 (2002).

[2] J. M. De Teresa, Agnès Barthélémy, Albert Fert, Jean Pierre Contour, François Montaigne, and P. Seneor, Science **286**, 507 (1999).

[3] M. Martin and E. Fromm, J. Alloys Compd. **258**, 7 (1997).

[4] H. Nair, M. J. Liszka, J. E. Gatt, and C. D. Baertsch, J. Phys. Chem. C **112**, 1612 (2008).

[5] G. Aguila, F. Gracia, J. Cortes, and P. Araya, Appl. Catal., B **77**, 325 (2008).

[6] W. Xue, X. Shi, M. Hua, and Y. Li, Appl. Surf. Sci. **253**, 6118 (2007).
[7] P. Juzon, M. Ziemnicka, S. Chevalier, K. Przybylski, and J. P. Larpin, Appl. Surf. Sci. **253**, 4928 (2007).
[8] A. B. Belonoshko, A. Rosengren, and G. Hultquist, Surf. Sci. **600**, 4796 (2006).
[9] R. P. Frankenthal, R. B. Van Dover, and D. J. Siconolfi, Appl. Phys. Lett. **51**, 542 (1987).
[10] R. L. Orban, M. Lucaci, M. Rosso, and M. A. Grande, Adv. Mater. Res. **23**, 273 (2007).
[11] L. P. H. Jeurgens, W. G. Sloof, F. D. Tichelaar, C. G. Borsboom, and E. J. Mittemeijer, Appl. Surf. Sci. **144-145**, 11 (1999).
[12] L. P. H. Jeurgens, W. G. Sloof, F. D. Tichelaar, and E. J. Mittemeijer, Phys. Rev. B **62**, 4707 (2000).
[13] L. P. H. Jeurgens, W. G. Sloof, F. D. Tichelaar, and E. J. Mittemeijer, J. Appl. Phys. **92**, 1649 (2002).
[14] P. Lamparter and R. Kniep, Physica B **234-236**, 405 (1997).
[15] K. Fueki and H. Ishibashi, J. Electrochem. Soc. **108**, 306 (1961).
[16] H. J. Grabke, Intermetallics **7**, 1153 (1999).
[17] S. Ulrich, N. Nilius, and H.-J. Freund, Surf. Sci. **601**, 4603 (2007).
[18] P. B. Balbuena, D. Altomare, N. Vadlamani, S. Bingi, L. A. Agapito, and J. M. Seminario, J. Phys. Chem. A **108**, 6378 (2004).
[19] Z. Gu and P. B. Balbuena, J. Phys. Chem. C **111**, 9877 (2007).
[20] K. Reuter and M. Scheffler, Phys. Rev. Lett. **90**, 046103 (2003).
[21] M. N. D. S. Cordeiro, A. S. S. Pinto, and J. A. N. F. Gomes, Surf. Sci. **601**, 2473 (2007).
[22] X.-Q. Gong, R. Raval, and P. Hu, Phys. Rev. Lett. **93**, 106104 (2004).
[23] C. J. Zhang, R. J. Baxter, P. Hu, A. Alavi, and M.-H. Lee, J. Chem. Phys. **115**, 5272 (2001).
[24] C. Zhang, P. Hu, and A. Alavi, J. Am. Chem. Soc. **121**, 7931 (1999).
[25] C. Bungaro, C. Noguera, P. Ballone, and W. Kress, Phys. Rev. Lett. **79**, 4433 (1997).
[26] E. Lundgren, G. Kresse, C. Klein, M. Borg, J. N. Andersen, M. De Santis, Y. Gauthier, C. Konvicka, M. Schmid, and P. Varga, Phys. Rev. Lett. **88**, 246103 (2002).
[27] D. Marx and J. Hutter, in *Modern Methods and Algorithms of Quantum Chemistry*, NIC Series (John von Neumann Institute for Computing, Julich, 2000).
[28] A. Hasnaoui, O. Politano, J. M. Salazar, and G. Aral, Phys. Rev. B **73**, 035427 (2006).
[29] A. Hasnaoui, O. Politano, J. M. Salazar, G. Aral, R. K. Kalia, A. Nakano, and P. Vashishta, Surf. Sci. **579**, 47 (2005).
[30] S. Ogata and T. J. Campbell, J. Phys.: Condens. Matter **10**, 11449 (1998).
[31] T. Campbell, R. K. Kalia, A. Nakano, P. Vashishta, S. Ogata, and S. Rodgers, Phys. Rev. Lett. **82**, 4866 (1999).
[32] T. J. Campbell, G. Aral, S. Ogata, R. K. Kalia, A. Nakano, and P. Vashishta, Phys. Rev. B **71**, 205413 (2005).
[33] D. Starodub, T. Gustafsson, and E. Garfunkel, Surf. Sci. **552**, 199 (2004).
[34] G. Gutierrez and B. Johansson, Phys. Rev. B **65**, 104202 (2002).
[35] X. W. Zhou, H. N. G. Wadley, J.-S. Filhol, and M. N. Neurock, Phys. Rev. B **69**, 035402 (2004).
[36] X. W. Zhou and H. N. G. Wadley, J. Phys.: Condens. Matter **17**, 3619 (2005).
[37] A. K. Rappe and W. A. Goddard, J. Phys. Chem. **95**, 3358 (1991).
[38] F. H. Streitz and J. W. Mintmire, Phys. Rev. B **50**, 11996 (1994).
[39] W. X. Li, L. Österlund, E. K. Vestergaard, R. T. Vang, J. Matthiesen, T. M. Pedersen, E. Lægsgaard, B. Hammer, and F. Besenbacher, Phys. Rev. Lett. **93**, 146104 (2004).
[40] D. S. Mainardi, S. R. Calvo, A. P. J. Jansen, J. J. Lukkien, and P. B. Balbuena, Chem. Phys. Lett. **382**, 553 (2003).
[41] S. Jaatinen, J. Blomqvist, P. Salo, A. Puisto, M. Alatalo, M. Hirsimäki, M. Ahonen, and M. Valden, Phys. Rev. B **75**, 075402 (2007).
[42] S. Jaatinen, M. Rusanen, and P. Salo, Surf. Sci. **601**, 1813 (2007).
[43] J. C. Yang, E. Schumann, H. Müllejans, and M. Rühle, J. Phys. D **29**, 1716 (1996).
[44] P. Gassmann, R. Franchy, and H. Ibach, Surf. Sci. **319**, 95 (1994).
[45] H. Isern and G. R. Castro, Surf. Sci. **211–212**, 865 (1989).
[46] R. M. Jaeger, H. Kuhlenbeck, H. J. Freund, M. Wuttig, W. Hoffmann, R. Franchy, and H. Ibach, Surf. Sci. **259**, 235 (1991).
[47] A. Y. Lozovoi, A. Alavi, and M. W. Finnis, Phys. Rev. Lett. **85**, 610 (2000).
[48] P. Gaßmann, R. Franchy, and H. Ibach, J. Electron Spectrosc. Relat. Phenom. **64-65**, 315 (1993).
[49] X. W. Zhou, H. N. G. Wadley, R. A. Johnson, D. J. Larson, N. Tabat, A. Cerezo, A. K. Petford-Long, G. D. W. Smith, P. H. Clifton, R. L. Martens, and T. F. Kelly, Acta Mater. **49**, 4005 (2001).
[50] M. W. Finnis and J. E. Sinclair, Philos. Mag. A **50**, 45 (1984).
[51] H. Okamoto, J. Phase Equilib. **14**, 257 (1993).
[52] P. Nash, M. F. Singleton, and J. L. Murray, in *Phase Diagrams of Binary Nickel Alloys*, edited by P. Nash (ASM International, Materials Park, OH, 1991), Monograph Series on Alloy Phase Diagrams, 3-11.
[53] P. P. Ewald, Ann. Phys. **369**, 253 (1921).
[54] L. Zhu and A. E. DePristo, J. Catal. **167**, 400 (1997).
[55] L. Zhu, R. Wang, T. S. King, and A. E. DePristo, J. Catal. **167**, 408 (1997).
[56] L. Zhu and A. E. DePristo, J. Chem. Phys. **102**, 5342 (1995).
[57] D. S. Mainardi and P. B. Balbuena, Langmuir **17**, 2047 (2001).
[58] S. K. R. S. Sankaranarayanan, V. R. Bhethanabotla, and B. Joseph, Phys. Rev. B **71**, 195415 (2005).
[59] S.-P. Huang and P. B. Balbuena, J. Phys. Chem. B **106**, 7225 (2002).
[60] S. K. R. S. Sankaranarayanan, V. R. Bhethanabotla, and B. Joseph, Phys. Rev. B **72**, 195405 (2005).
[61] S. K. R. S. Sankaranarayanan, V. R. Bhethanabotla, and B. Joseph, Phys. Rev. B **76**, 134117 (2007).
[62] S. K. R. S. Sankaranarayanan, V. R. Bhethanabotla, and B. Joseph, J. Phys. Chem. C **111**, 2430 (2007).
[63] S. K. R. S. Sankaranarayanan, V. R. Bhethanabotla, and B. Joseph, Phys. Rev. B **74**, 155441 (2006).
[64] X. W. Zhou and H. N. G. Wadley, Phys. Rev. B **71**, 054418 (2005).
[65] D. J. Evans and B. L. Holian, J. Chem. Phys. **83**, 4069 (1985).
[66] M. P. Allen and D. J. Tildesley, *Computer Simulation of Liquids* (Clarendon, Oxford, 1987).
[67] K. R. Lawless, Rep. Prog. Phys. **37**, 231 (1974).
[68] L. S. Caputi, S. L. Jiang, A. Amoddeo, and R. Tucci, Phys. Rev. B **41**, 8513 (1990).
[69] J. M. Haile, *Molecular Dynamics Simulations: Elementary*

Methods (Wiley, New York, 1992).

[70] A. Atkinson, Rev. Mod. Phys. **57**, 437 (1985).

[71] A. R. Kortan and R. L. Park, Phys. Rev. B **23**, 6340 (1981).

[72] M. W. Finnis, A. Y. Lozovoi, and A. Alavi, Annu. Rev. Mater. Res. **35**, 167 (2005).

[73] M. Yoshitake, B. Mebarki, and T. T. Lay, Surf. Sci. **511**, L313 (2002).

[74] A. Stierle, F. Renner, R. Streitel, H. Dosch, W. Drube, and B. C. Cowie, Science **303**, 1652 (2004).

[75] R. Franchy, J. Masuch, and P. Gassmann, Appl. Surf. Sci. **93**, 317 (1996).

[76] D. R. Lide, *CRC Handbook of Chemistry and Physics* (CRC, Boca Raton, FL, 1995).

[77] U. Bardi, A. Atrei, and G. Rovida, Surf. Sci. **268**, 87 (1992).

[78] J. Kelber, N. Magtoto, C. Vamala, M. Jain, D. R. Jennison, and P. A. Schultz, Surf. Sci. **601**, 3464 (2007).

[79] D. R. Jennison, C. Verdozzi, P. A. Schultz, and M. P. Sears, Phys. Rev. B **59**, R15605 (1999).

[80] G. Kresse, M. Schmid, E. Napetschnig, M. Shishkin, L. Koehler, and P. Varga, Science **308**, 1440 (2005).

[81] A. Stierle, V. Formoso, F. Comin, and R. Franchy, Surf. Sci. **467**, 85 (2000).

[82] A. Stierle, V. Formoso, F. Comin, G. Schmitz, and R. Franchy, Physica B (Amsterdam) **283**, 208 (2000).

[83] P. Gassmann, R. Franchy, and H. Ibach, J. Electron Spectrosc. Relat. Phenom. **64-65**, 315 (1993).

[84] A. Mulligan, V. Dhanak, and M. Kadodwala, Langmuir **21**, 8312 (2005).

[85] D. R. Jennison and A. Bogicevic, Faraday Discuss. **114**, 45 (1999).

[86] D. R. Jennison and A. Bogicevic, Surf. Sci. **464**, 108 (2000).